sensors

MDPI

Article

Adaptive Magnetocardiography Denoising via Tent Chaotic Dream Optimization and Bidirectional LSTM

Kaiming Zhao, Jiayun Wang, Junping Duan and Binzhen Zhang *

State Key Laboratory of Extreme Environment Optoelectronic Dynamic Testing Technology and Instrument, North University of China, Taiyuan 030051, China; b20210605@st.nuc.edu.cn (K.Z.); wangjiayun@nuc.edu.cn (J.W.); duanjunping@nuc.edu.cn (J.D.)
* Correspondence: zhangbinzhen@nuc.edu.cn

Abstract

Magnetocardiography (MCG) is a non-invasive technique for recording the heart's weak magnetic fields, but its clinical value in cardiac assessment is often undermined by strong acquisition noise. Existing denoising schemes generally suffer from three practical issues: manual parameter tuning, inadequate preservation of diagnostic waveform details, and poor adaptability to varying noise conditions. To address these challenges, a hybrid framework termed TCDOA-VMD-BiLSTM is proposed in this work. In this framework, a Tent chaotic map-enhanced Dream Optimization Algorithm (TCDOA) automatically searches for the optimal parameters of Variational Mode Decomposition (VMD), enabling reliable separation of signal and noise. The resulting Intrinsic Mode Functions (IMFs) are then fed into a Bidirectional Long Short-Term Memory (BiLSTM) network, which learns a direct mapping from noisy IMFs to clean signals and captures temporal dependencies in both forward and reverse directions. The proposed framework was compared against five representative approaches: Finite Impulse Response (FIR) filter, RPSEMD with hard and soft thresholding (RPSEMD-Hard and RPSEMD-Soft), Symplectic Geometry Mode Decomposition combined with Wavelet Thresholding (SGMD-WT), and a Deep Residual Shrinkage Network (DRSN). Experimental results show that TCDOA-VMD-BiLSTM achieves the best overall performance across all tested conditions. On the simulated MCG dataset, the proposed method reaches a maximum Signal to Noise Ratio improvement (SNR_{imp}) of 23.68 dB, a maximum Cosine Similarity (CosSim) of 0.998, and a minimum Root Mean Square Error (RMSE) of 0.0135 pT. For clinical MCG signals with different noise severity levels (mild, moderate, and severe), the proposed method consistently produces the highest SNR_{imp} and CosSim together with the lowest RMSE among compared algorithms. These findings indicate that the proposed framework effectively suppresses complex noise in MCG signals while preserving waveform features essential for subsequent clinical interpretation.

Keywords: magnetocardiography; signal denoising; dream optimization algorithm; tent chaotic map; bidirectional LSTM

Academic Editor: Christian Baumgartner

Received: 26 September 2026
Revised: 17 November 2026
Accepted: 18 November 2026
Published: 26 November 2026

Copyright: © 2026 by the author. Licensee MDPI, Basel, Switzerland. This article is an open access article distributed under the terms and conditions of the Creative Commons Attribution (CC BY) license.

1. Introduction

Cardiovascular Disease (CAD) remains the leading cause of death worldwide. By 2050, the global burden of CAD is projected to exceed 35.6 million deaths annually,

placing increasing pressure on healthcare systems and underscoring the urgent need for early, accurate, and non-invasive cardiac assessment tools [1,2].

Among emerging cardiac monitoring techniques, Magnetocardiography (MCG) has attracted considerable attention. MCG measures the weak magnetic fields generated by cardiac electrical activity without requiring contact with the body [3–5]. In contrast to Electrocardiography (ECG), which depends on electrode–skin contact and is sensitive to physiological variability and external interference, MCG avoids contact-related signal degradation and directly captures the magnetic field produced by intracardiac currents [6,7]. High-sensitivity sensors such as Superconducting Quantum Interference Devices (SQUIDs) allow MCG to resolve field changes as small as 10^{-17} T, and sensor arrays further enable spatiotemporal mapping of cardiac magnetic fields for source localization [8–10]. Figure 1 illustrates a clinically deployed MCG acquisition system and the spatial distribution of its sensor array over the precordium. These features make MCG promising for detecting myocardial ischemia, inflammatory cardiomyopathy, and fetal congenital heart disease.

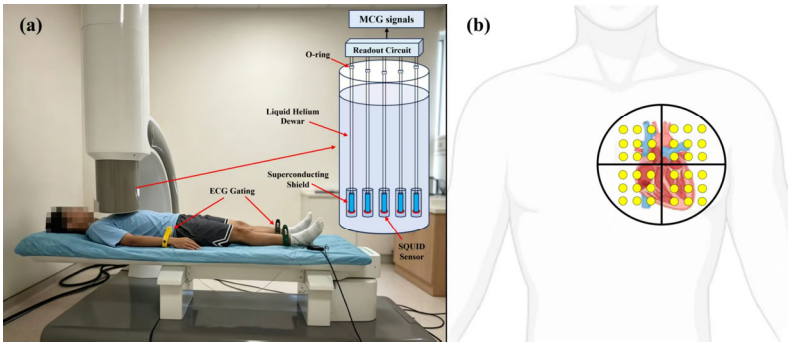


Figure 1. SQUID-based magnetocardiography acquisition system and the sensor array distribution on the precordial region. (**a**) Schematic of the clinical MCG data acquisition setup. (**b**) The 36-channel sensor array distribution.

However, the clinical value of MCG is limited by its low signal amplitude and high susceptibility to noise. Baseline wander from respiration, power-line interference, muscle artifacts, and environmental electromagnetic noise often overlap with the diagnostic frequency band and obscure the P wave, QRS complex, and T wave. Effective denoising is therefore a prerequisite for reliable MCG interpretation [11,12].

A wide range of denoising strategies has been explored. Conventional filters, including high-pass, notch filters, and adaptive filters, are simple and effective for specific noise types but struggle when noise and signal overlap in frequency [13–16]. Fourier and wavelet-based methods can suppress periodic and non-stationary noise, but their performance depends on the empirical choice of basis functions and thresholds [17,18]. Statistical methods such as principal component analysis and independent component analysis separate signal and noise based on statistical properties, but they rely on assumptions of stationarity and independence that are rarely satisfied in clinical MCG recordings [19–21]. Decomposition-based methods, particularly Empirical Mode Decomposition (EMD), can adaptively decompose the signal into Intrinsic Mode Functions (IMFs). However, these methods are highly sensitive to noise and prone to mode mixing [22–26]. To overcome these limitations, Variational Mode Decomposition (VMD) has emerged as a more robust alternative. It reformulates decomposition as a constrained variational problem, which mitigates mode mixing and improves robustness on non-stationary signals [27–30]. However, VMD requires two parameters to be set in advance: the number of modes K and the penalty factor α. Manual selection of these parameters is subjective, time-consuming,

and difficult to generalize across recordings with different noise levels and morphological characteristics.

In recent years, deep learning techniques have been explored for denoising in various non-stationary signal domains. For instance, the Deep Residual Shrinkage Network (DRSN) integrates residual learning with adaptively learned soft-thresholding to suppress noise while preserving waveform details, and has been successfully applied to geomagnetic data and EEG signal denoising [31,32]. However, these data-driven models still require substantial labeled training data and lack an explicit mechanism for modeling long-range temporal dependencies, which limits their ability to preserve subtle diagnostic features such as low-amplitude P waves under heavy noise. Recently, more sophisticated deep learning architectures have been introduced specifically for physiological signal denoising. For instance, Xing et al. proposed a Multi-Level Gated U-Net for denoising MCG signals [12]. Hu et al. developed a lightweight U-Net model for ECG denoising [33]. Additionally, attention-based mechanisms, such as the Convolutional Block Attention Autoencoder, have been successfully applied to preserve diagnostic features while suppressing noise [34].

To address these two limitations, namely manual parameter tuning in decomposition-based methods and insufficient temporal modeling in data-driven methods, this paper proposes a hybrid MCG denoising framework called TCDOA-VMD-BiLSTM. A Tent chaotic map is introduced to enhance Dream Optimization Algorithm (DOA), forming the Tent Chaotic Dream Optimization Algorithm (TCDOA). To replace random initialization, a deterministically ergodic sequence is provided by the Tent map. This approach enhances population diversity and search-space coverage while preserving the core memory and sharing mechanisms of the DOA. TCDOA is then used to adaptively optimize the VMD parameters (K, α), with the minimum envelope entropy of the resulting IMFs as the fitness function. The optimized VMD decomposes the MCG signal into a set of well-separated IMFs. Finally, a Bidirectional Long Short-Term Memory (BiLSTM) network performs component-wise denoising and end-to-end reconstruction, capturing temporal dependencies in both forward and reverse directions and avoiding manual IMF selection.

Experiments on simulated and clinical MCG signals show that the proposed method outperforms five representative denoising methods across noise levels and subjects. The recovered waveforms retain the P, QRS and T features required for clinical interpretation.

2. Materials and Methods

This section describes the proposed TCDOA-VMD-BiLSTM denoising framework. The framework consists of three main stages: adaptively optimizing the VMD parameters via TCDOA, decomposing the noisy MCG signal into IMFs using the optimized VMD, and performing component-wise denoising and reconstruction of the IMFs with a BiLSTM network. The overall workflow is illustrated in Figure 2.

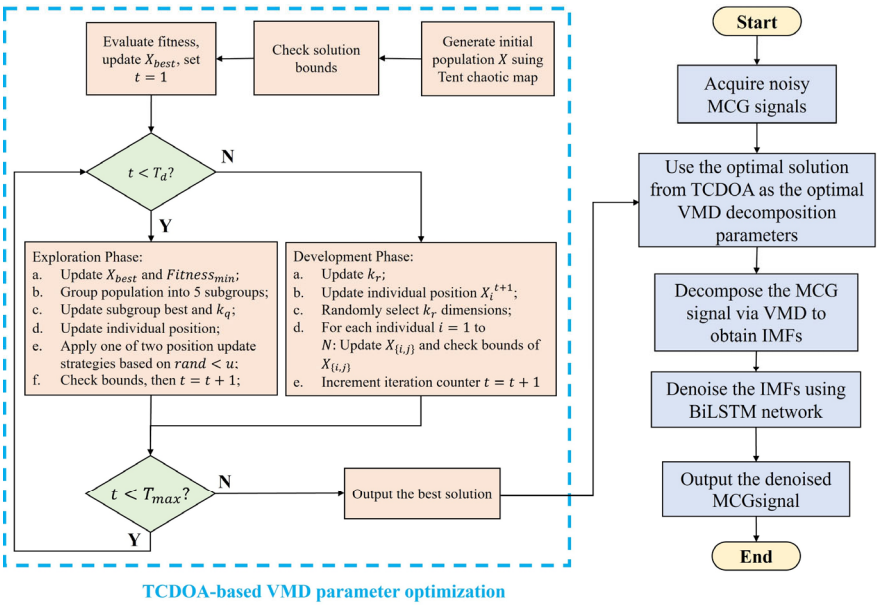


Figure 2. Overall workflow of the proposed TCDOA-VMD-BiLSTM denoising framework.

2.1. VMD

VMD is a non-recursive signal decomposition method proposed by Dragomiretskiy and Zosso [27]. It decomposes a signal into a set of band-limited IMFs by solving a constrained variational problem. Each IMF is defined as:

$$u_k(t) = A_k(t)\cos\left(\Phi_k(t)\right), \tag{1}$$

where $A_k(t)$ is the instantaneous amplitude and $\Phi_k(t)$ is the phase function. The instantaneous frequency $\omega_k(t) = d\Phi_k(t)/dt$ varies slowly with respect to $\Phi_k(t)$, so that each $u_k(t)$ can be regarded as a narrowband signal. The decomposition is formulated as:

$$\min_{\{u_k\},\{\omega_k\}} \left\{ \sum_{k=1}^{K} \left\| \partial_t \left[\left(\delta(t) + \frac{j}{\pi t} \right) * u_k(t) \right] e^{-j\omega_k t} \right\|_2^2 \right\}, \tag{2}$$

subject to:

$$\sum_{k=1}^{K} u_k(t) = f(t), \tag{3}$$

where $f(t)$ is the input signal, $\{u_k\} = \{u_1, u_2, \ldots, u_K\}$ are the IMFs, $\{\omega_k\} = \{\omega_1, \omega_2, \ldots, \omega_K\}$ are the center frequencies, and K is the number of modes.

To solve this constrained problem, a quadratic penalty factor α and a Lagrangian multiplier $\lambda(t)$ are introduced, yielding the extended Lagrangian:

$$L(\{u_k\}, |\omega_k|, \lambda) = \alpha \sum_{k=1}^{K} \left\| \partial_t \left[\left(\delta(t) + \frac{j}{\pi t} \right) * u_k(t) \right] e^{-j\omega_k t} \right\|_2^2 + \left\| f(t) - \sum_{k=1}^{K} u_k(t) \right\|_2^2 + \langle \lambda(t), f(t) - \sum_{k=1}^{K} u_k(t) \rangle, \tag{4}$$

The Alternating Direction Method of Multipliers (ADMM) is then used to iteratively update u_k, ω_k, and λ until convergence. The update equations are:

$$\hat{u}_k^{n+1}(\omega) = \frac{\hat{f}(\omega) - \sum_{i \neq k} \hat{u}_i(\omega) + \frac{\hat{\lambda}(\omega)}{2}}{1 + 2\alpha(\omega - \omega_k)^2}, \tag{5}$$

$$\omega_k^{n+1} = \frac{\int_0^\infty \omega |\hat{u}_k^{n+1}(\omega)|^2 d\omega}{\int_0^\infty |\hat{u}_k^{n+1}(\omega)|^2 d\omega}, \tag{6}$$

$$\hat{\lambda}^{n+1}(\omega) = \hat{\lambda}^n(\omega) + \tau \left(\hat{f}(\omega) - \sum_k \hat{u}_k^{n+1}(\omega) \right), \tag{7}$$

where τ is the update step size. The iteration stops when:

$$\frac{\sum_k \|\hat{u}_k^{n+1} - \hat{u}_k^n\|_2^2}{\|\hat{u}_k^n\|_2^2} < \varepsilon, \tag{8}$$

The parameters K and α strongly affect the decomposition quality but are difficult to set manually. In this work, they are adaptively optimized by TCDOA.

2.2. TCDOA

2.2.1. Tent Chaotic Map

Tent chaotic map was introduced by Habutsu et al. in 1991 for cryptographic applications [35]. To overcome the limitations of random initialization, a Tent chaotic map is introduced to replace the random initialization in DOA. Random initialization may lead to uneven coverage of the search space, unstable convergence across different runs, and premature convergence to local optima, especially in multimodal optimization problems such as VMD parameter tuning. The Tent map is a one-dimensional piecewise linear chaotic map defined as:

$$z_{n+1} = \begin{cases} \frac{z_n}{\beta}, & 0 < z_n \le \beta \\ \frac{1-z_n}{1-\beta}, & \beta < z_n < 1 \end{cases}, \tag{9}$$

where $\beta \in (0,1)$ is the control parameter and $z_n \in (0,1)$ is the chaotic variable. When $\beta = 0.499$, the map exhibits strong ergodicity and a uniform invariant density. The Tent map is used to generate an initial chaotic sequence $\{z_1, z_2, \ldots, z_N\}$. The first 100 iterations are discarded to eliminate transient effects. The initial position of the i-th candidate solution is then mapped to the search space as:

$$X_{i,j}^{(0)} = LB_j + z_i \times (UB_j - LB_j), \tag{10}$$

where B_j and UB_j are the lower and upper bounds of the j-th dimension, respectively. Compared with random initialization, Tent-map-based initialization provides a deterministically ergodic and more uniform distribution of initial solutions, which improves population diversity and reduces the risk of premature convergence. In practical floating-point arithmetic, a Tent map with $\beta = 0.5$ is prone to collapsing into a fixed point due to finite precision. To mitigate this, a safeguard mechanism is applied. Specifically, the control parameter is set to $\beta = 0.499$ to prevent exact periodic orbits while maintaining ergodicity. Furthermore, a small perturbation ($\epsilon = 10^{-8}$) is introduced whenever the chaotic variable approaches zero or a periodic point.

2.2.2. Dream Optimization Algorithm

The DOA is a population-based metaheuristic proposed in 2025 [36]. It is inspired by three characteristics of human dreams: memory retention, forgetting and supplementation, and dream sharing. Memory retention preserves promising solutions during iterations, forgetting and supplementation act as a perturbation operator that enhances exploration, and dream sharing enables information exchange among individuals to accelerate convergence. Through the interaction of these three mechanisms, DOA balances exploration and exploitation during optimization.

Let the population be denoted as $\boldsymbol{X} = \{\boldsymbol{x}_1, \boldsymbol{x}_2, \ldots, \boldsymbol{x}_N\}$, where N is the population size and $\boldsymbol{x}_i \in \mathbb{R}^D$ is the position of the i-th candidate solution in a D-dimensional search space. The fitness of each solution is $f(\boldsymbol{x}_i)$. The main steps of DOA are as follows:

- **Initialization**. A population of N candidate solutions is randomly generated in the search space:

$$x_i^{(0)} = LB + r_i \odot (UB - LB), i = 1,2,\dots,N, \tag{11}$$

where LB and UB are the lower and upper bounds, $r_i \in [0,1]^D$ is a random vector, and $\odot$ denotes element-wise multiplication.

- **Memory retention**. A portion of the current population is retained as memory based on fitness. The memory set $M^{(t)}$ at iteration t is formed by selecting the top N_m individuals:

$$M^{(t)} = \left\{x_{(1)}^{(t)}, x_{(2)}^{(t)}, \dots, x_{(N_m)}^{(t)}\right\}, \tag{12}$$

where $x_{(1)}^{(t)}, \dots, x_{(N_m)}^{(t)}$ are the individuals sorted by fitness in ascending order, and $N_m = \lfloor p_m N \rfloor$ with p_m being the memory retention rate.

- **Forgetting and supplementation**. Some individuals are discarded, and new individuals are generated to replace them:

$$x_i^{(t+1)} = x_{\text{new}}, i \in \mathcal{D}^{(t)}, \tag{13}$$

where $\mathcal{D}^{(t)}$ is the set of discarded individuals, and x_{new} is a newly generated solution:

- **Dream sharing.** Information is exchanged among individuals to guide the population toward better regions:

$$x_i^{(t+1)} = x_i^{(t)} + r_1 \odot \left(x_{\text{best}}^{(t)} - x_i^{(t)}\right) + r_2 \odot \left(x_j^{(t)} - x_k^{(t)}\right), \tag{14}$$

where $x_{\text{best}}^{(t)}$ is the best solution found so far, $x_j^{(t)}$ and $x_k^{(t)}$ are two randomly selected individuals ($j \neq k \neq i$), and $r_1, r_2 \in [0,1]^D$ are random vectors.

- **Termination.** The memory retention, forgetting and supplementation, and dream sharing steps are repeated until the maximum number of iterations $T_{\max}$ is reached. The best solution found is returned as the final output.

Despite its effectiveness, DOA relies on random initialization according to Equation 11, which may lead to uneven coverage of the search space and unstable convergence, especially in multimodal optimization problems such as VMD parameter tuning.

2.2.3. TCDOA Procedure

By integrating the Tent chaotic map into DOA, the TCDOA is obtained. The key difference between DOA and TCDOA lies in the initialization strategy: DOA generates its initial population using random numbers (Equation 11), whereas TCDOA replaces this with a Tent chaotic map, which produces a deterministically ergodic and more uniformly distributed initial population. All other mechanisms, including memory retention, forgetting and supplementation, and dream sharing, remain unchanged. The procedure of TCDOA is summarized as follows:

1. Initialization: Generate N initial solutions using the Tent map according to Equation 10.
2. Fitness evaluation: Evaluate the fitness of each candidate solution.
3. Memory retention: Select the top individuals based on fitness.
4. Forgetting and supplementation: Replace poor individuals with newly generated ones.
5. Dream sharing: Exchange information among individuals to update positions.
6. Termination: Repeat steps 2–5 until the maximum number of iterations $T_{\max}$ is

reached.

The output is the optimal parameter set (K, α) for VMD. In this work, TCDOA is used to optimize the VMD parameters K and α. The fitness function is defined as the minimum envelope entropy of the IMFs, which reflects the sparsity of the signal components. For a set of K IMFs, the envelope entropy is calculated as:

$$E_p = -\sum_{j=1}^{N} p_j \ln p_j, \tag{15}$$

where $p_j = \frac{a(j)}{\sum_{j=1}^{N} a(j)}$, $a(j)$ is the envelope of the IMF obtained via the Hilbert transform, p_j is the normalized envelope, and N is the signal length. The mean envelope entropy is:

$$E_{\text{MEE}} = \frac{1}{K}\sum_{k=1}^{K} E_{p,k}, \tag{16}$$

The optimization problem is:

$$\min_{(K,\alpha)} E_{\text{MEE}}(K, \alpha), K_{\min} \le K \le K_{\max}, \alpha_{\min} \le \alpha \le \alpha_{\max}, \tag{17}$$

The detailed procedure is as follows:

1. Set the search ranges $K \in [K_{\min}, K_{\max}]$ and $\alpha \in [\alpha_{\min}, \alpha_{\max}]$.
2. Initialize the TCDOA population using the Tent map.
3. For each candidate (K, α), decompose the noisy MCG signal using VMD and compute the mean envelope entropy.
4. Update the population using the memory retention, forgetting and supplementation, and dream sharing mechanisms of DOA.
5. Repeat steps 3–4 until the maximum number of iterations is reached.
6. Output the optimal parameters (K, α).

Furthermore, to rigorously evaluate the robustness and avoid stochastic bias, both the standard DOA and our proposed TCDOA were independently executed 30 times to minimize the envelope entropy for VMD parameter optimization. Figure 3a shows the statistical distribution of the final fitness values over these 30 independent runs. As observed, TCDOA achieves a significantly lower mean envelope entropy with a much narrower distribution and smaller standard deviation, whereas the standard DOA yields a higher mean value with a much larger variance. Figure 3b presents a representative single-run convergence comparison. The results demonstrate that TCDOA not only converges faster but also escapes local optima earlier, ultimately reaching a significantly lower minimum envelope entropy. This statistically confirms that the Tent chaotic map enhancement effectively improves the global search capability and convergence stability of the DOA.

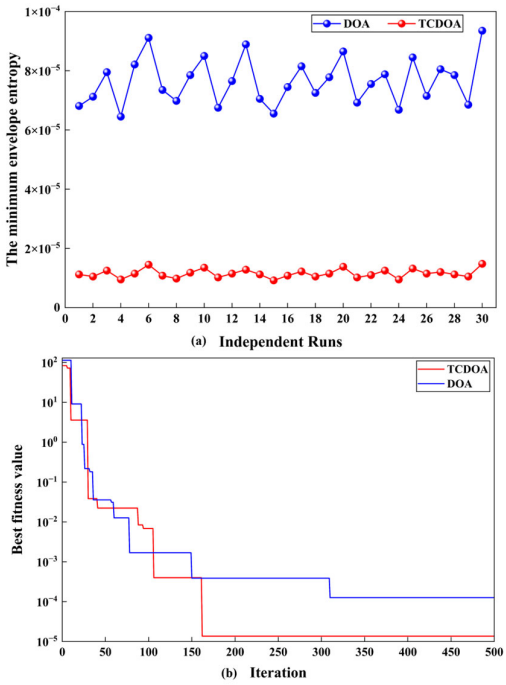


Figure 3. Optimization performance evaluation of standard DOA and TCDOA. (**a**) Statistical distribution of the final minimum envelope entropy over 30 independent runs. (**b**) Representative single-run convergence curves.

2.3. BiLSTM-Based Denoising and Reconstruction

After VMD with the optimized parameters, the noisy MCG signal is decomposed into K IMFs. These IMFs are then fed into a BiLSTM network for component-wise denoising and end-to-end reconstruction. Long Short-Term Memory (LSTM) is a recurrent neural network designed to address the vanishing gradient problem. It contains three gating units: the input gate, the forget gate, and the output gate [37]. The LSTM updates are:

$$i_t = \sigma(W_i[h_{t-1}, x_t] + b_i), \tag{18}$$

$$f_t = \sigma\big(W_f[h_{t-1}, x_t] + b_f\big), \tag{19}$$

$$o_t = \sigma(W_o[h_{t-1}, x_t] + b_o), \tag{20}$$

$$\tilde{C}_t = \tanh(W_C[h_{t-1}, x_t] + b_C), \tag{21}$$

$$C_t = f_t \odot C_{t-1} + i_t \odot \tilde{C}_t, \tag{22}$$

$$h_t = o_t \odot \tanh(C_t), \tag{23}$$

where $\sigma(\cdot)$ is the sigmoid function, $\odot$ is element-wise multiplication, and W and b are learnable parameters.

A standard LSTM only processes the sequence in the forward direction. A BiLSTM processes the sequence in both forward and backward directions and concatenates the two hidden states [38–40]:

$$\overrightarrow{h_t} = \mathrm{LSTM}\big(x_t, \overrightarrow{h_{t-1}}\big), \tag{24}$$

$$\overleftarrow{h_t} = \mathrm{LSTM}\left(x_t, \overleftarrow{h_{t+1}}\right), \tag{25}$$

$$h_t = \left[\overrightarrow{h_t}; \overleftarrow{h_t}\right], \tag{26}$$

This bidirectional structure captures temporal dependencies from both past and future contexts, which is well suited to quasi-periodic MCG signals.

The architecture of the proposed BiLSTM network is illustrated in Figure 4. The input to the network is a sequence of IMFs obtained from the TCDOA-optimized VMD, denoted as:

$$X = [x_1, x_2, \ldots, x_N], \tag{27}$$

where $x_t \in \mathbb{R}^K$ contains the K IMF components at time step t, and N is the signal length. Therefore, the input dimension is $K \times N \times 1$.

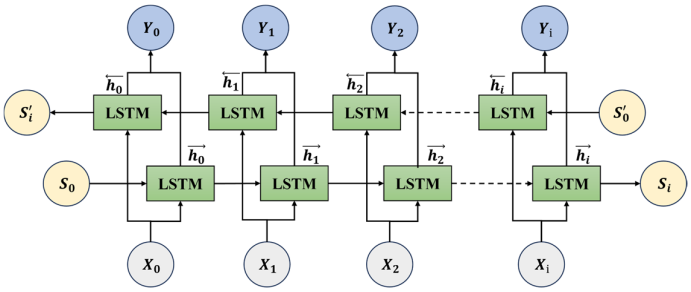


Figure 4. Architecture of the BiLSTM network.

The network consists of the following layers in sequence:

- Sequence Input Layer: Accepts the normalized IMFs with input size K, formatted as $[K, N, 1]$. Each IMF is standardized to zero mean and unit variance before being fed into the network, which prevents components with large amplitudes from dominating the training process.
- BiLSTM Layer: Contains 50 hidden units in each direction. Unlike a unidirectional LSTM, the BiLSTM layer reads the sequence in both directions and concatenates the two hidden states, so that each output depends on both past and future context. The output dimension is $[100, N, 1]$.
- Fully Connected Layer: Projects the BiLSTM output to a 50-dimensional feature space, reducing the dimensionality of the concatenated bidirectional features and facilitating the subsequent regression task.
- Dropout Layer: A dropout rate of 0.2 is applied for regularization. This randomly deactivates 20% of the neurons during training, which reduces the risk of overfitting given the limited size of the clinical MCG dataset.
- Regression Layer: Produces the final denoised signal $\hat{y} \in \mathbb{R}^N$ as a sequence-to-sequence output, with output dimension $[1, N, 1]$.

This bidirectional context is well suited to quasi-periodic MCG signals, in which the P, QRS and T waves have a regular morphology. The bidirectional structure, combined with the dropout regularization, enables the network to suppress noise while preserving diagnostically critical waveform features. The network is trained in a supervised manner, where the clinician-confirmed clean segments are used as the reference signals. During training, the mean squared error (MSE) between the network output and the clean reference is minimized using the Adam optimizer, so that the network learns a direct mapping from noisy IMFs to clean MCG waveforms.

2.4. Evaluation Indicators

To quantitatively evaluate the denoising performance, three indicators are used: Signal-to-Noise Ratio improvement (SNR_{imp}), Cosine Similarity (CosSim), and Root Mean Square Error (RMSE). Let $s = [s_1, s_2, \ldots, s_N]$ denote the clean reference signal, $\hat{s} = [\hat{s}_1, \hat{s}_2, \ldots, \hat{s}_N]$the denoised signal, and $h = [h_1, h_2, \ldots, h_N]$the noisy signal, where $N$is the number of samples [41,42]. The three indicators are defined as:

$$\mathrm{SNR}_{\mathrm{imp}}\,(s, \hat{s}) = 10\log_{10}\frac{\sum_{j=1}^{N}(h_j - s_j)^2}{\sum_{j=1}^{N}(\hat{s}_j - s_j)^2}, \tag{28}$$

$$\mathrm{CosSim}\,(s, \hat{s}) = \frac{\sum_{j=1}^{N} s_j \hat{s}_j}{\sqrt{\sum_{j=1}^{N} s_j^2}\sqrt{\sum_{j=1}^{N} \hat{s}_j^2}}, \tag{29}$$

$$\mathrm{RMSE}(s, \hat{s}) = \sqrt{\frac{1}{N}\sum_{j=1}^{N}\left(\hat{s}_j - s_j\right)^2}, \tag{30}$$

A higher SNR_{imp} and CosSim, together with a lower RMSE, indicate better denoising performance.

3. Results and Discussion

3.1. Experimental Setup

To quantitatively assess the denoising performance, a simulated MCG signal was constructed to provide a noise-free reference for quantitative evaluation. The signal had a duration of 10 s and a sampling frequency of 1000 Hz. The P wave, QRS complex, and T wave were modeled as Gaussian-shaped components, and the pure MCG signal was generated by summing these components for each heartbeat with a fixed RR interval of 1.0 s. The resulting signal was scaled to a suitable amplitude range.

Three types of noise were then added to the clean signal: Baseline Wander (BW), Power-line interference (PLI), and Gaussian white noise. All amplitudes are expressed in pT. The BW was modeled as a random walk generated by cumulative summation of Gaussian random values, which was then mean-centered and normalized to a maximum amplitude of 5 pT. The PLI was modeled as a 50 Hz sinusoidal signal with an amplitude of 10 pT. The Gaussian white noise was modeled with a standard deviation of 8 pT. The noisy signal was constructed as the sum of the pure MCG signal and the three noise components, without additional scaling factors. The waveforms of the simulated pure signal, the three types of noise, and the resulting noisy signal are shown in Figure 5.

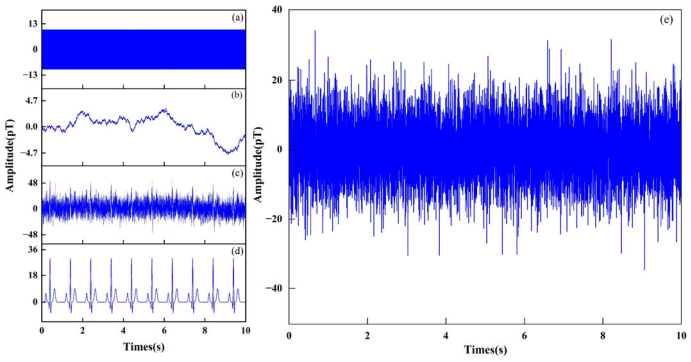


Figure 5. Simulated MCG signal and its noise components; (**a**) pure MCG; (**b**) BW; (**c**) PLI; (**d**) Gaussian noise; (**e**) noisy MCG.

To further validate the proposed method on real MCG recordings, clinical MCG signals were collected at Suzhou Dushu Lake Hospital between June 2024 and March 2025 using a 36-channel SQUID system. The dataset included 60 subjects, of whom a portion were CAD patients diagnosed by coronary angiography and the remainder had other conditions. Each recording lasted 60 s at a sampling frequency of 1000 Hz, and 10-s segments were extracted for processing. For each subject, a clean reference segment was identified on the basis of a stable baseline, distinguishable PQRST morphology, and independent confirmation by two experienced clinicians. One representative subject is shown in Figure 6.

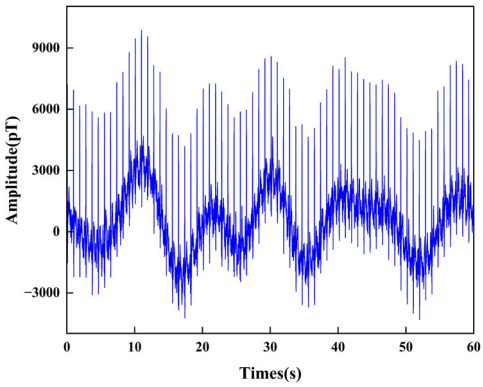


Figure 6. Measured clinical MCG signal.

To prevent data leakage, the clinical dataset was split at the subject level. Of the 60 subjects, 40 were assigned to training and 20 were held out for testing. Within the 40 training subjects, 8 were further reserved for validation, leaving 32 for training. The three roles are therefore disjoint at the subject level, and no segment from a subject appears in a role other than that subject's. Training pairs were formed only from the training subjects, by adding the simulated composite noise (baseline wander, power-line interference, and Gaussian white noise) to their clean reference segments, with the clean segments as labels.

The proposed method consists of a TCDOA-based optimizer and a BiLSTM denoiser. In TCDOA, the population size was 30 and the maximum number of iterations was 500, while the search ranges of K and α were $[2, 20]$ and $[100, 5000]$, respectively. The Tent map control parameter was $\beta = 0.499$. To eliminate the transient effect of the initial value and ensure a uniformly distributed chaotic sequence for population initialization, the first 100 chaotic iterations were discarded. The BiLSTM denoiser contained one BiLSTM layer with 50 hidden units in each direction, followed by a fully connected layer with 50 units and a dropout layer with a rate of 0.2. Training was performed using the Adam optimizer with a learning rate of 0.001 and a batch size of 64 for a maximum of 1000 epochs, with early stopping based on validation loss. The optimal K and α values obtained by TCDOA for the simulated and clinical MCG signals are reported in Sections 3.2 and 3.3, respectively.

The proposed TCDOA-VMD-BiLSTM was compared with five methods, and the parameter settings of these methods are described as follows:

- Finite Impulse Response (FIR) filter [43,44]: A band-pass filter with a passband of 0.5–45 Hz, a filter order of 200, and a Hamming window was applied with zero-phase filtering.
- Regenerative Phase Shifted Empirical Mode Decomposition with Soft Thresholding (RPSEMD-Soft) [45,46]: For RPSEMD, the amplitude of the added sinusoidal assisted signal was set to 0.2 times the standard deviation of the input signal, the number of sifting iterations was 10, and the decomposition was terminated when the standard

deviation between two consecutive sifting results fell below 0.2. The resulting IMFs were denoised by soft thresholding, with the threshold for each IMF estimated from the median absolute deviation of the first IMF.

- Regenerative Phase Shifted Empirical Mode Decomposition with Hard Thresholding (RPSEMD-Hard): The same RPSEMD configuration as in RPSEMD-Soft was used, except that the resulting IMFs were denoised by hard thresholding instead of soft thresholding.
- Symplectic Geometry Mode Decomposition combined with Wavelet Thresholding (SGMD-WT) [47]: For SGMD-WT, the embedding dimension was set to 30, and the termination condition was based on a frequency similarity threshold of 0.01. The resulting SGCs were denoised by wavelet thresholding using the db4 wavelet with 6 decomposition levels and soft thresholding.
- Deep Residual Shrinkage Network (DRSN) [31,32]: The DRSN consisted of 10 residual shrinkage building units, each containing two convolutional layers with 64 filters of size 3, batch normalization, ReLU activation, and an adaptively learned soft-thresholding operation. The network was trained using the Adam optimizer with a learning rate of 0.001 and a batch size of 64 for 200 epochs, with early stopping based on the validation loss.

All comparison methods used the same training and testing split as the proposed method.

3.2. Simulation Experiment Results

3.2.1. Denoising Performance on Simulated MCG Signals

The convergence characteristics of TCDOA for simulated MCG signal optimization are illustrated in Figure 7. As shown in Figure 7a, the penalty factor α starts from an initial value near 2966 and stabilizes at 2934.64 after approximately 10 iterations, with only minor fluctuations thereafter. As shown in Figure 7b, the mode number K is initialized as 7 and converges to 6 within several iterations. The rapid stabilization of both parameters suggests that TCDOA efficiently identifies a suitable parameter combination, which is consistent with the improved initial population distribution provided by the Tent chaotic map.

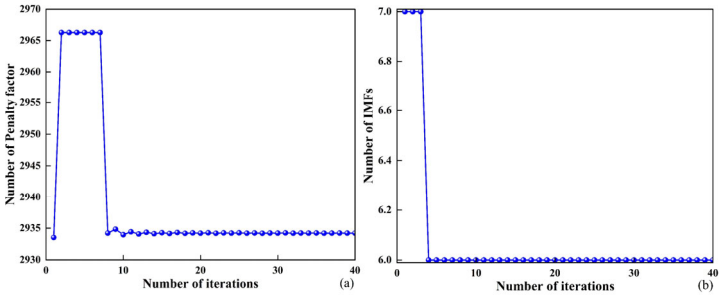


Figure 7. Convergence curves of the parameters for the simulated MCG signal. (**a**) Iterative variation of the penalty factor α. (**b**) Evolution of the mode number K.

Figure 8 presents the IMFs obtained by VMD under the optimal parameters optimized by TCDOA, along with their frequency spectra. For the simulated signal, IMF1–IMF3 contain the broadband high-frequency noise, IMF4 contains the power-line interference, and IMF5–IMF6 contain the low-frequency cardiac components; the PQRST morphology is carried mainly by IMF6, together with the residual baseline wander. As can be seen in Figure 8(a), the IMF6 waveform still exhibits a slow fluctuation superimposed on the MCG morphology. Compared with conventional VMD using manually preset

parameters, the optimized VMD yields IMFs with clearer frequency separation and alleviates the mode-mixing phenomenon.

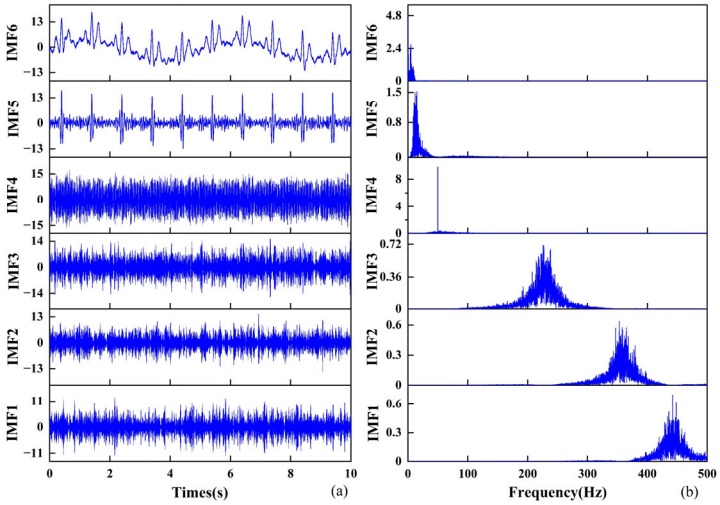


Figure 8. IMFs of the simulated MCG signal obtained by TCDOA-optimized VMD. (**a**) Time-domain waveforms of each IMF component; (**b**) corresponding frequency-domain spectra of each IMF.

A visual comparison of the denoised waveforms obtained by the proposed method and the five competing algorithms is provided in Figure 9, together with the noisy signal and the clean reference. The waveform recovered by TCDOA-VMD-BiLSTM matches the clean reference most closely. The P, QRS and T waves are clearly distinguishable, the R-peak amplitudes are preserved, and the baseline stays stable over the 10 s recording. The FIR filter only partially suppresses the high-frequency noise. Residual noise is still visible around the P-wave and T-wave regions, and the baseline wander is not fully removed, which leads to a noticeable low-frequency fluctuation in the recovered waveform. RPSEMD-Soft removes most of the noise, but the P wave becomes blurred and the R-peak amplitude is attenuated, indicating that useful low-amplitude components are partially removed together with the noise. RPSEMD-Hard preserves more waveform details than the soft-thresholding variant, but it introduces spurious oscillations in the TP segment, which may be misinterpreted as physiological activity. SGMD-WT performs better than FIR and the two RPSEMD variants. The QRS complexes are well recovered and the baseline is largely corrected, but residual noise is still observable near the T wave, and the T-wave morphology is slightly distorted. DRSN effectively stabilizes the baseline, but it introduces noticeable distortion in the QRS complex and slightly reduces the T-wave amplitude, suggesting that the network tends to over-smooth the sharp transitions of the MCG waveform. Overall, the proposed TCDOA-VMD-BiLSTM achieves the best balance between noise suppression and waveform preservation, which is consistent with the quantitative results reported in the following section.

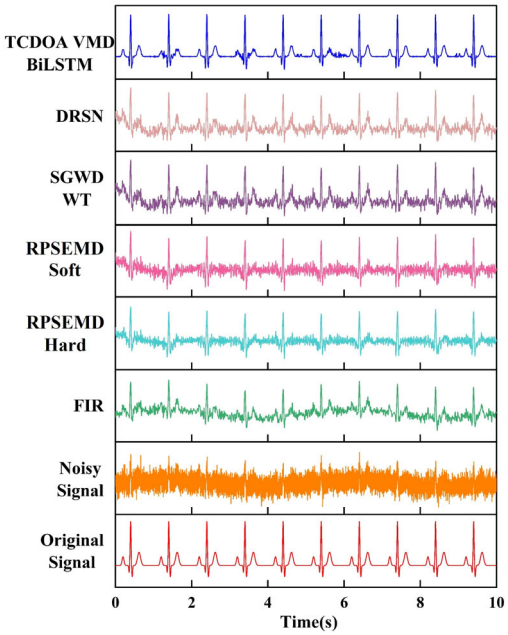


Figure 9. Denoising results of various methods on the simulated MCG signal.

Quantitative metrics for all competing methods are summarized in Table 1. TCDOA-VMD-BiLSTM achieves the best overall performance, with the highest SNR_{imp} of 18.65 dB, the highest CosSim of 0.967, and the lowest RMSE of 0.024 pT. DRSN ranks second, yielding an SNR_{imp} of 16.47 dB, a CosSim of 0.945, and an RMSE of 0.036 pT. RPSEMD-Soft and RPSEMD-Hard follow, with SNR_{imp} values of 12.15 dB and 10.42 dB and RMSE values of 0.058 pT and 0.072 pT, respectively. SGMD-WT and the FIR filter show the weakest performance, with SNR_{imp} values of 10.05 dB and 10.12 dB and RMSE values of 0.079 pT and 0.082 pT, respectively. It should be noted that baseline wander is included as one of the composite noise components in the simulated signal. Therefore, the quantitative results reported in Table 1 implicitly reflect the ability of each method to suppress low-frequency baseline drift. Despite the presence of baseline wander, the proposed method reduces the RMSE to 0.024 pT, whereas the FIR filter and SGMD-WT leave RMSE values of 0.082 pT and 0.079 pT, respectively. This contrast indicates that VMD optimized by TCDOA can effectively separate low-frequency baseline drift from the valid MCG signal band, which contributes to the improved denoising performance of the proposed method.

Table 1. Quantitative comparison of different denoising methods on the simulated MCG signal.

Methods	SNR_{imp}	CosSim	RMSE
TCDOA-VMD-BiLSTM	18.65	0.967	0.024
FIR	10.12	0.875	0.082
RPSEMD-Hard	10.42	0.905	0.072
RPSEMD-Soft	12.15	0.918	0.058
SGMD-WT	10.05	0.891	0.079
DRSN	16.47	0.945	0.036

3.2.2. Robustness Under Different Input SNR Levels

To further validate the robustness of the proposed denoising algorithm, Gaussian white noise with different noise levels was added to the clean simulated MCG signals. The input SNR was set from −10 dB to 10 dB with a step of 5 dB. The results for all compared methods are listed in Table 2.

Table 2. Quantitative comparison of various denoising methods on the simulated MCG signals under different input SNR levels.

Input SNR	Metrics	TCDOA-VMD-BiLSTM	FIR	RPSEMD-Hard	RPSEMD-Soft	SGMD-WT	DRSN
−10 dB	SNR_{imp}	13.42	7.42	9.85	10.62	9.24	11.85
	CosSim	0.926	0.812	0.856	0.882	0.838	0.895
	RMSE	0.0325	0.092	0.078	0.068	0.084	0.056
−5 dB	SNR_{imp}	15.65	9.68	11.24	12.05	10.52	13.28
	CosSim	0.948	0.862	0.902	0.918	0.885	0.915
	RMSE	0.0255	0.078	0.066	0.058	0.072	0.048
0 dB	SNR_{imp}	18.35	10.85	12.62	13.42	11.85	14.68
	CosSim	0.978	0.905	0.932	0.945	0.922	0.947
	RMSE	0.0205	0.065	0.055	0.048	0.060	0.040
5 dB	SNR_{imp}	20.05	11.92	13.85	14.68	12.95	16.02
	CosSim	0.992	0.932	0.952	0.962	0.945	0.971
	RMSE	0.0165	0.054	0.045	0.040	0.050	0.033
10 dB	SNR_{imp}	23.68	12.85	14.92	15.85	13.95	17.35
	CosSim	0.998	0.949	0.968	0.975	0.958	0.982
	RMSE	0.0135	0.045	0.038	0.033	0.042	0.027

Across the entire range of input SNR conditions, the proposed method consistently achieves the highest SNR_imp and CosSim together with the lowest RMSE among all competing algorithms. The performance advantage is particularly pronounced under severe noise conditions at −10 dB and −5 dB input SNR. In these low-SNR scenarios, TCDOA-VMD-BiLSTM outperforms the second-best method, DRSN, by approximately 1.6–2.4 dB in terms of SNR_{imp}, while maintaining a CosSim improvement of about 0.03 and an RMSE reduction of about 0.02 pT compared with DRSN. This observation indicates that the adaptive VMD parameter optimization implemented by TCDOA can achieve reliable signal–noise separation even when the noise energy is high. The bidirectional sequence modeling of BiLSTM further helps recover MCG waveform details buried in heavy noise.

As the input SNR increases, all methods exhibit improved CosSim and reduced RMSE, which is consistent with the expectation that denoising becomes easier when the noise level decreases. Nevertheless, TCDOA-VMD-BiLSTM still maintains a clear performance margin over the other algorithms, even in the high-input-SNR case (10 dB). At 10 dB input SNR, the proposed method achieves an SNR_{imp} of 23.68 dB, which is 6.33 dB higher than that of DRSN and more than 10 dB higher than those of FIR and SGMD-WT. In terms of CosSim, the proposed method reaches 0.998, very close to the ideal value of 1, indicating that the recovered waveform is almost identical to the clean reference. These results demonstrate that the hybrid framework has strong generalization capability for both high-noise and relatively clean simulated MCG recordings.

3.3. Clinical MCG Experimental Results

3.3.1. Denoising Performance for Clinical Subjects

To further validate the practicability of TCDOA-VMD-BiLSTM on clinically acquired MCG signals, clinical MCG data collected using a 36-channel SQUID system were tested. Since clinical MCG recordings cannot provide an absolute noise-free reference, a clinician-confirmed clean segment was used as the pseudo ground truth for quantitative evaluation. Specifically, the segment was selected according to three criteria: (i) a stable baseline with no visible drift, (ii) clearly distinguishable PQRST morphology, and (iii) independent

confirmation by two experienced clinicians. This pseudo ground truth was used only as a relative reference for computing SNR_{imp}, CosSim, and RMSE, and all quantitative comparisons were performed under the same reference.

Furthermore, to address the temporal misalignment between different clinical segments, an R-peak synchronization strategy was applied. The R-peaks of both the clean reference and the noisy segments were detected, and the noisy segments were temporally aligned to the clean reference based on these peaks before calculating the quantitative metrics. The severity grouping (mild, moderate, severe) was subsequently determined based on the input SNR computed from these strictly aligned segments. The pseudo ground truth is used only as a relative reference. Because the reference and the analyzed segment are taken from the same recording of the same subject, they share the sensor position and the subject state, and the R-peak alignment removes the temporal offset between them. The reference is identical for all six methods, so the comparison is paired; it is never used as a training target for the subject being evaluated. The absolute values of SNR_{imp}, CosSim and RMSE should therefore not be read as absolute denoising accuracy, but as a ranking of the methods under a common reference.

Figure 10 presents the iterative convergence curves of the hyperparameters α and K yielded by TCDOA for the representative clinical MCG sample. As shown in Figure 10a, the penalty factor α remains at its initial value of 2870 during the first seven iterations and then drops sharply to 2850.02, after which it stays stable for the remaining iterations. As shown in Figure 10b, the mode number K is initialized as 7 and decreases to 6 at the eighth iteration, remaining unchanged thereafter. Both hyperparameters converge within a limited number of iterations and then remain stable, demonstrating that TCDOA can efficiently search suitable VMD parameters even for clinical MCG signals contaminated by complex mixed noise.

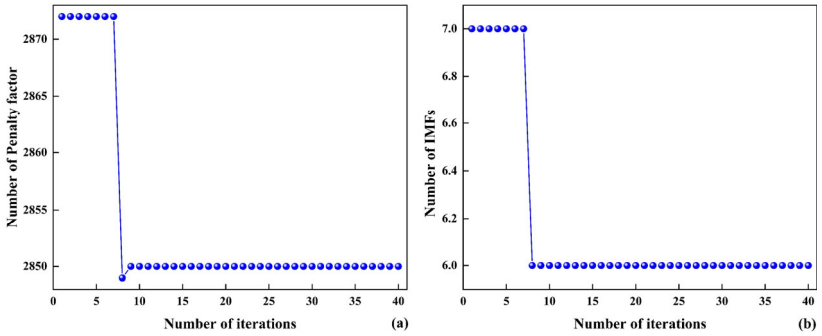


Figure 10. Convergence curves of the parameters for the clinical MCG signal. (**a**) Iterative variation of the penalty factor α. (**b**) Evolution of the mode number K.

Figure 11 depicts the IMF components obtained by VMD with TCDOA-optimized parameters for the clinical MCG signal. Figure 11a shows the time-domain waveform of each IMF, and Figure 11b presents the corresponding frequency spectra. The IMFs exhibit clear frequency-domain separation. IMF1 and IMF2 are dominated by high-frequency noise above 200 Hz. IMF3–IMF5 contain the main physiological components of the clinical MCG signal, including the P wave, QRS complex, and T wave, and their waveforms show clear periodic cardiac activity. IMF6 corresponds to the low-frequency baseline drift, which appears as a slow fluctuation in the time domain. Compared with conventional VMD using manually preset parameters, the optimized VMD yields clearer frequency separation and alleviates the mode-mixing phenomenon, thereby improving the decomposition performance for noisy clinical MCG signals.

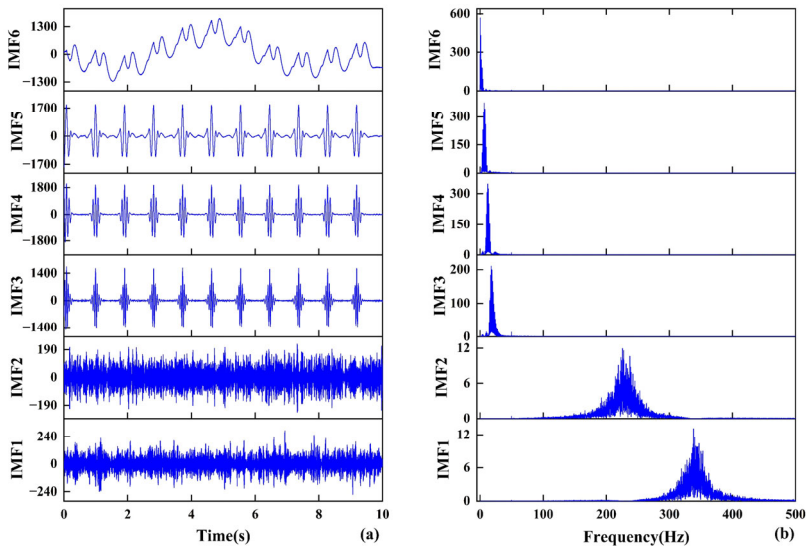


Figure 11. IMFs of the clinical MCG signal obtained by TCDOA-optimized VMD. (**a**) Time-domain waveforms of each IMF component; (**b**) corresponding frequency-domain spectra of each IMF.

Figure 12 compares the denoised time-domain waveforms obtained by the proposed framework and the five competing algorithms on the representative clinical MCG sample, together with the noisy recording and the pseudo ground truth. The waveform recovered by TCDOA-VMD-BiLSTM shows the best visual quality, with clearly distinguishable P waves, QRS complexes, and T waves, well-preserved R-peak amplitudes, and a stable baseline. Its waveform almost overlaps with the pseudo ground truth, which is consistent with the highest SNR_{imp} of 20.66 dB, the highest CosSim of 0.985, and the lowest RMSE of 0.0185 pT reported in Table 3.

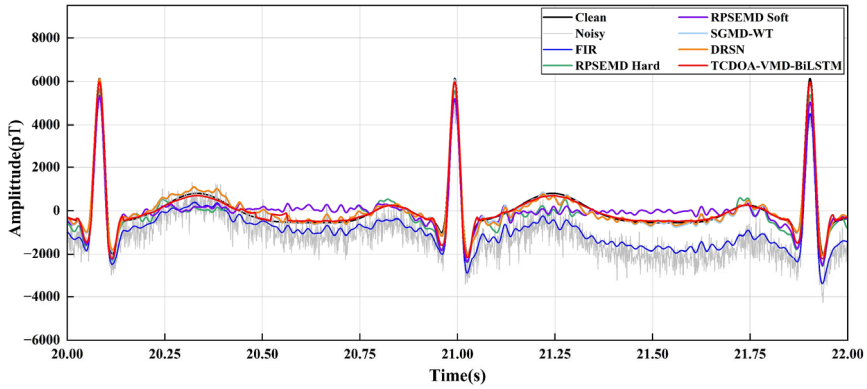


Figure 12. Denoising results of various methods on the clinical MCG signal.

In contrast, the other methods suffer from different degrees of residual noise or waveform distortion. SGMD-WT and the FIR filter perform worst. SGMD-WT leaves residual noise across the cardiac cycle (SNR_{imp} 7.85 dB, RMSE 0.0780 pT), and the FIR filter removes neither baseline wander nor high-frequency noise (9.85 dB, 0.0650 pT). RPSEMD-Hard and RPSEMD-Soft provide intermediate performance. RPSEMD-Soft achieves a slightly higher SNR_{imp} (13.68 dB) and a lower RMSE (0.0485 pT) than RPSEMD-Hard (12.15 dB and 0.0520 pT), but its CosSim is lower (0.901 vs. 0.925), indicating that soft thresholding removes more noise at the cost of blurring the P wave and attenuating the R-peak amplitude. RPSEMD-Hard preserves the waveform shape better, but introduces spurious oscillations in the TP segment.

DRSN ranks second among all methods, with an SNR_{imp} of 17.54 dB, a CosSim of 0.955, and an RMSE of 0.0325 pT. It effectively stabilizes the baseline, but introduces noticeable distortion in the QRS complex and slightly reduces the T-wave amplitude, suggesting that the network tends to over-smooth the sharp transitions of the MCG waveform. Overall, TCDOA-VMD-BiLSTM achieves the best balance between noise suppression and waveform preservation, which is consistent with the quantitative results in Table 3.

Table 3. Quantitative comparison of various denoising methods on the clinical MCG signal.

Methods	SNR_{imp}	CosSim	RMSE
TCDOA-VMD-BiLSTM	20.66	0.985	0.0185
FIR	9.85	0.899	0.0650
RPSEMD-Hard	12.15	0.925	0.0520
RPSEMD-Soft	13.68	0.901	0.0485
SGMD-WT	7.85	0.842	0.0780
DRSN	17.54	0.955	0.0325

The assignment differs from the simulated case because the clinical recording has a much stronger baseline drift, which occupies the lowest-frequency mode; the cardiac content is therefore distributed over IMF3–IMF5. Because the BiLSTM consumes all K modes jointly, the method does not rely on a fixed mode assignment.

3.3.2. Denoising Performance for Clinical Samples with Different Noise Severity

The 20 held-out subjects were analyzed at three noise levels. For each subject, a clean reference segment and three 10-s target segments were selected from the same 60-s recording, and the three targets were assigned to the mild, moderate and severe strata according to their input SNR, computed with that subject's own clean reference as the signal-power baseline: mild (SNR > 5 dB), moderate (0 dB < SNR ≤ 5 dB) and severe (SNR ≤ 0 dB). This gives 60 segments in total and n = 20 per group, with each subject contributing exactly one segment to each group and no segment from a training subject. Representative raw clinical MCG waveforms for the three severity levels are shown in Figure 13.

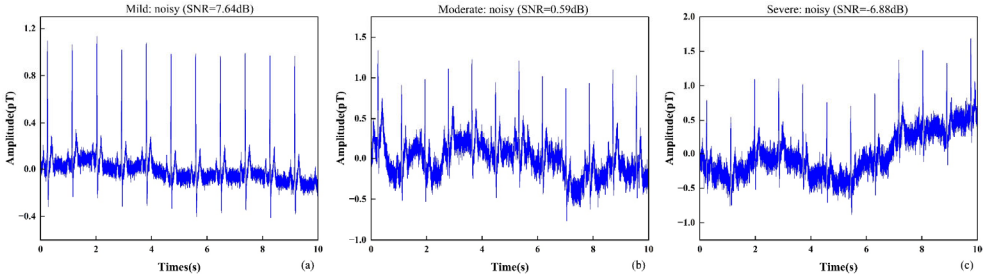


Figure 13. Representative clinical MCG waveforms with mild, moderate, and severe noise. (**a**) Mild noise. (**b**) Moderate noise. (**c**) Severe noise.

The denoising results of the three representative clinical segments are illustrated in Figure 14. In the mild noise group (Figure 14a), all methods produce visually acceptable waveforms, but the FIR filter and RPSEMD-Soft still leave noticeable residual noise in the TP segment, while SGMD-WT and RPSEMD-Hard show slight fluctuations near the T wave. In contrast, the waveform recovered by TCDOA-VMD-BiLSTM is highly consistent with the clean reference, with clear PQRST morphology and a stable baseline. These observations are consistent with the quantitative results in Table 4, where the proposed method achieves the highest SNR_{imp} (16.52 ± 1.15 dB), the highest CosSim (0.979 ± 0.013), and the lowest RMSE (0.022 ± 0.005 pT) in the mild group.

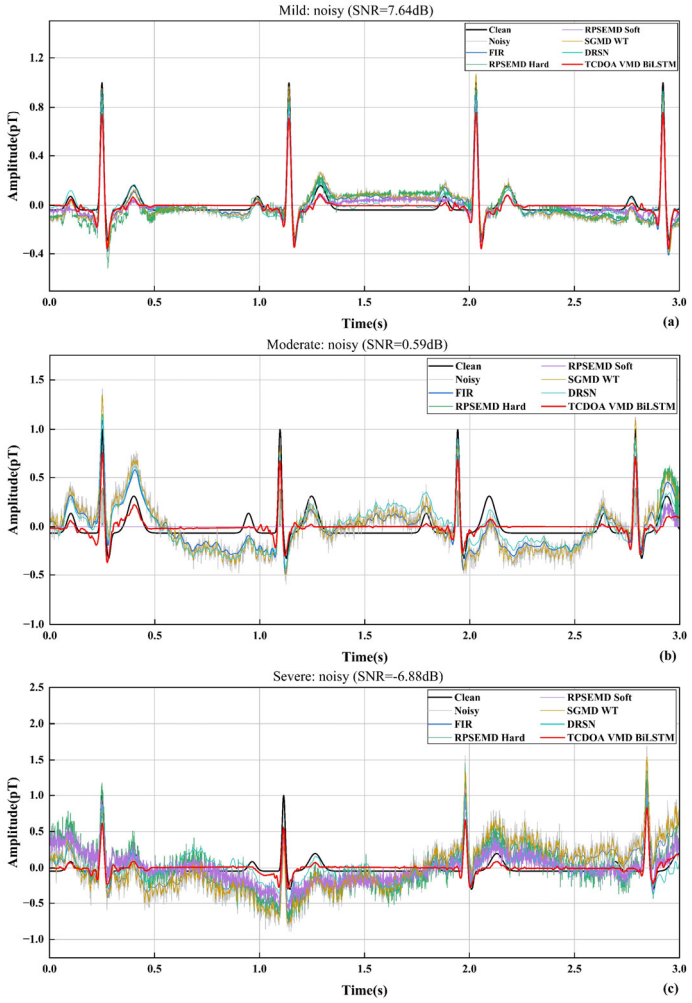


Figure 14. Denoising results of various methods on clinical MCG signals with different noise severity levels. (**a**) Mild noise (SNR = 7.64 dB). (**b**) Moderate noise (SNR = 0.59 dB). (**c**) Severe noise (SNR = −6.88 dB).

Table 4. Quantitative comparison of various denoising methods on clinical MCG signals under mild, moderate, and severe noise conditions. (Mean ± Std).

Noise Severity	Metrics	TCDOA-VMD-BiLSTM	FIR	RPSEMD-Hard	RPSEMD-Soft	SGMD-WT	DRSN
Mild	SNR_{imp}	16.52 ± 1.15	10.65 ± 0.80	12.20 ± 1.10	13.85 ± 1.30	11.10 ± 0.95	15.56 ± 1.25
	CosSim	0.979 ± 0.013	0.895 ± 0.030	0.925 ± 0.028	0.925 ± 0.022	0.905 ± 0.030	0.960 ± 0.018
	RMSE	0.022 ± 0.005	0.054 ± 0.010	0.045 ± 0.009	0.036 ± 0.008	0.051 ± 0.010	0.027 ± 0.006
Moderate	SNR_{imp}	13.45 ± 1.25	8.25 ± 0.70	9.60 ± 0.95	11.15 ± 1.15	8.50 ± 0.85	12.40 ± 1.20
	CosSim	0.945 ± 0.018	0.850 ± 0.036	0.880 ± 0.032	0.905 ± 0.025	0.850 ± 0.038	0.943 ± 0.022
	RMSE	0.032 ± 0.007	0.074 ± 0.013	0.063 ± 0.013	0.052 ± 0.011	0.072 ± 0.014	0.038 ± 0.008
Severe	SNR_{imp}	8.75 ± 1.35	5.46 ± 0.53	6.15 ± 0.75	7.40 ± 0.95	5.20 ± 0.65	8.10 ± 1.10

CosSim	0.895 ± 0.025	0.760 ± 0.042	0.795 ± 0.045	0.835 ± 0.038	0.770 ± 0.048	0.870 ± 0.030
RMSE	0.058 ± 0.009	0.132 ± 0.025	0.112 ± 0.020	0.092 ± 0.018	0.120 ± 0.024	0.065 ± 0.013

As the noise severity increases to the moderate group (Figure 14b), the FIR filter and RPSEMD-Soft still exhibit obvious baseline fluctuations, while SGMD-WT and DRSN introduce slight distortions in the QRS complex by attenuating the R-peak amplitude. In contrast, the proposed method maintains a distinguishable PQRST morphology. In Table 4, the proposed method still achieves the highest SNR_{imp} (13.45 ± 1.25 dB) and the lowest RMSE (0.032 ± 0.007 pT) in this group, while its CosSim (0.945 ± 0.018) is comparable to that of DRSN (0.943 ± 0.022).

The advantage of the proposed method becomes most prominent in the severe noise group (Figure 14c), where only the proposed method and DRSN maintain a discernible PQRST morphology. The other methods either retain substantial baseline wander or oversmooth the R peak, losing critical diagnostic information. The quantitative results in Table 4 further confirm this trend: the proposed method achieves an SNR_{imp} of 8.75 ± 1.35 dB, a CosSim of 0.895 ± 0.025, and an RMSE of 0.058 ± 0.009 pT, all of which are better than those of the competing methods, and the performance gap becomes larger as the noise level increases.

Across all three groups, the proposed method consistently yields the highest mean SNR_{imp} and CosSim together with the lowest mean RMSE, demonstrating its superior and stable denoising performance under varying clinical noise conditions.

To assess whether the performance gains are statistically robust, paired t-tests were performed separately for each noise-severity group, with the subject as the unit of analysis (n = 20 paired segments per group). The proposed method achieved a higher output SNR than DRSN in all three groups, and the largest of the three p-values was 0.016, which remains below 0.05 after Bonferroni correction for the three comparisons. These results indicate that the improvement is systematic rather than attributable to random variation.

3.3.3. Preservation of Diagnostic Features Across Multiple Subjects and Channels

To further address the clinical validity of the proposed algorithm across spatial and inter-subject variations, this study evaluated its performance in preserving the ST-T segment morphology across different subjects and multiple channels. Figure 15 presents the denoised ST-T segment waveforms for four different subjects, with two distinct channels shown for each. Specifically, (a),(b) display different channels from Subject 1; (c),(d) correspond to Subject 2; (e),(f) represent Subject 3; and (g),(h) are from Subject 4.

Because of the spatial heterogeneity of cardiac electrophysiology, the ST-T waveforms vary significantly among different channels and subjects. Under such complex spatial and inter-subject variations, traditional methods exhibit notable limitations: the FIR filter fails to eliminate severe baseline wander, and the RPSEMD methods introduce varying degrees of morphological distortion.

In contrast, the proposed TCDOA-VMD-BiLSTM consistently tracks the clean reference with high fidelity across all subplots. It accurately preserves critical diagnostic features, including the ST-segment elevation or depression and the T-wave polarity, without introducing artificial phase shifts or amplitude attenuation. The ST segment is a standard marker of myocardial ischemia, and preserving its morphology is therefore a prerequisite for downstream analysis. These observations indicate that the proposed method preserves ST-T morphology across subjects and channels; a diagnostic evaluation of CAD detection is beyond the scope of this denoising study and is left for future work.

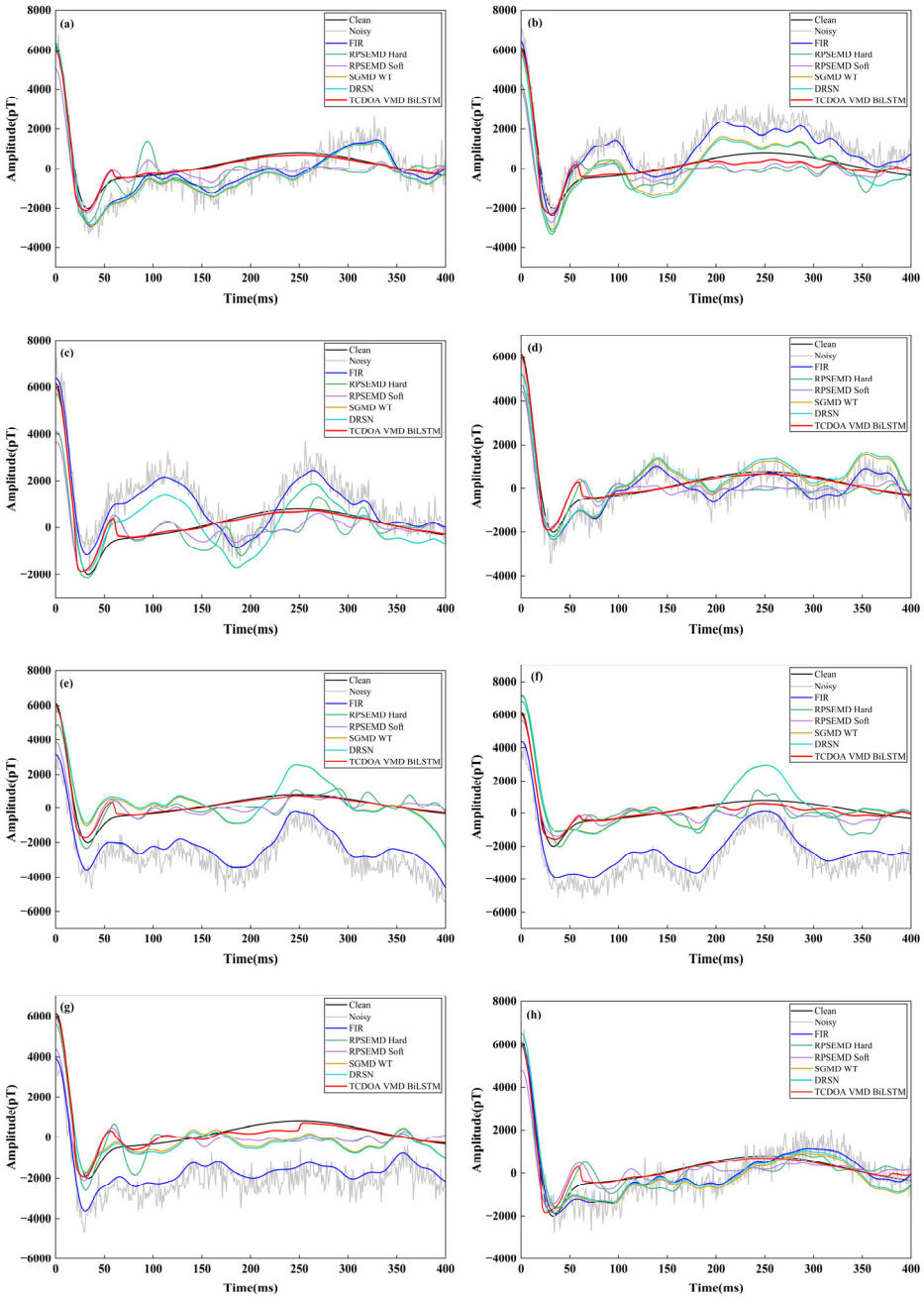


Figure 15. Preservation of ST-T segment morphology across multiple subjects and channels. (**a**,**b**) Channels from Subject 1; (**c**,**d**) Channels from Subject 2; (**e**,**f**) Channels from Subject 3; (**g**,**h**) Channels from Subject 4.

3.4. Ablation Study

To evaluate the contribution of each component in the proposed framework, an ablation study was conducted on the clinical MCG data. Five configurations were compared: (1) VMD-LSTM: VMD with manually set parameters ($K = 7, \alpha = 2568.52$), followed by a standard unidirectional LSTM; (2) VMD-BiLSTM: VMD with manually set parameters, followed by a BiLSTM; (3) DOA-VMD-BiLSTM: VMD optimized by the original DOA, followed by a BiLSTM; (4) TCDOA-VMD-LSTM: VMD optimized by TCDOA, followed by a standard unidirectional LSTM; and (5) TCDOA-VMD-BiLSTM: the complete

proposed framework. The quantitative results of the five configurations are presented in Table 5.

The results clearly demonstrate the effectiveness of each proposed component. VMD-BiLSTM improves SNR_{imp} from 15.45 to 16.32 dB and reduces RMSE from 0.0485 to 0.0420 pT relative to VMD-LSTM, which shows the benefit of bidirectional modeling. Similarly, TCDOA-VMD-BiLSTM improves SNR_{imp} from 19.98 to 20.66 dB and reduces RMSE from 0.0249 to 0.0185 pT relative to TCDOA-VMD-LSTM, so the BiLSTM contributes 0.68 dB and 0.0064 pT even with optimized VMD parameters.

Table 5. Ablation study of the proposed framework on the clinical MCG data.

Methods	SNR_{imp}	CosSim	RMSE
VMD-LSTM	15.45	0.935	0.0485
VMD-BiLSTM	16.32	0.948	0.0420
DOA-VMD-BiLSTM	18.75	0.970	0.0286
TCDOA-VMD-LSTM	19.98	0.979	0.0249
TCDOA-VMD-BiLSTM	20.66	0.985	0.0185

Building on this, replacing manual parameter selection with DOA-based optimization (VMD-BiLSTM → DOA-VMD-BiLSTM) raises the SNR_{imp} from 16.32 dB to 18.75 dB while lowering the RMSE from 0.0420 pT to 0.0286 pT. A further substitution of DOA with TCDOA (DOA-VMD-BiLSTM → TCDOA-VMD-BiLSTM) elevates the SNR_{imp} to 20.66 dB and reduces the RMSE to 0.0185 pT. This progression indicates that the Tent chaotic map improves the uniformity of the initial population and helps TCDOA avoid premature convergence, thereby yielding better VMD parameters than the original DOA.

Taken together, the full TCDOA-VMD-BiLSTM framework achieves the best performance across all metrics (highest SNR_{imp} and CosSim, lowest RMSE), demonstrating that the integration of TCDOA optimization and BiLSTM reconstruction is highly effective for clinical MCG denoising.

3.5. Computational Cost

All computations were performed on a laptop equipped with an Intel Core i9-13900HX CPU, 64 GB of RAM and an NVIDIA GeForce RTX 4060 GPU, running Windows 11 and MATLAB 2024b (PyTorch 2.1 with CUDA 12.1 for the deep learning models). The laptop was sourced from Lenovo, Beijing, China. VMD and TCDOA were executed on the CPU in double precision, and the BiLSTM network was trained and evaluated on the GPU. Each timing is the wall-clock time measured on the same 10-s segment (10,000 samples) and averaged over five repeated runs.

To evaluate the computational efficiency, the processing time of the proposed framework and the comparison methods was measured on a 10-s MCG segment (10,000 samples). The optimization time, inference time, and total processing time of each method are presented in Table 6.

As shown in Table 6, the conventional FIR filter achieves the shortest total time (1.2 s), because it involves only fixed-coefficient filtering without any iterative decomposition or learning process. SGMD-WT requires 2.8 s, while the RPSEMD variants require 6.5–6.8 s due to the iterative sifting and wavelet thresholding operations. DRSN, a deep learning method, needs 65 s for training and 10.5 s for inference, giving the longest total time (75.5 s) of all methods compared.

Table 6. Computational cost of the proposed framework and the comparison methods.

Methods	Optimization Time (s)	Inference Time (s)	Total Time (s)
TCDOA-VMD-BiLSTM	18(TCDOA)+ 43(Training)	5.2	66.2
FIR	-	1.2	1.2
RPSEMD-Hard	-	6.5	6.5
RPSEMD-Soft	-	6.8	6.8
SGMD-WT	-	2.8	2.8
DRSN	65	10.5	75.5

The proposed TCDOA-VMD-BiLSTM requires 18 s for the TCDOA optimization stage, 43 s for the offline BiLSTM network training, and 5.2 s for VMD and BiLSTM inference. This results in a total time of 66.2 s for the initial processing. This total is longer than that of the conventional methods (FIR, SGMD-WT and the RPSEMD variants). It is, however, shorter than that of DRSN (75.5 s), whose cost depends strongly on the training set. Both the TCDOA optimization and the BiLSTM training are performed only once, offline, and the pre-trained model and optimized parameters can then be reused for subsequent segments of the same recording. The online cost is therefore 5.2 s per 10-s segment on the hardware described above, i.e., about 0.5× the segment duration. This is sufficient for near-real-time analysis in a store-and-process workflow, but it does not by itself constitute real-time operation: in the present implementation a segment is processed only after it has been fully acquired, and the TCDOA parameters are re-optimised for each new recording. Streaming deployment with bounded latency would require a sliding-window formulation, parameter reuse across segments, and further acceleration of the VMD and BiLSTM stages. We therefore describe the present system as suitable for offline and near-real-time clinical analysis rather than as a real-time monitor.

4. Conclusions

In this work, a hybrid MCG denoising framework named TCDOA-VMD-BiLSTM is developed. The core strategy involves the adaptive determination of VMD parameters via a TCDOA, thereby ensuring more reliable signal-noise separation. Each resulting IMF is then processed by a BiLSTM network in an end-to-end fashion, which avoids the need for manually selecting valid IMFs and thus reduces information loss. The denoised IMFs are finally recombined to reconstruct the clean MCG waveform. This design addresses three practical issues in MCG denoising: sensitivity to complex noise, difficulty in parameter tuning, and insufficient preservation of diagnostically relevant waveform features.

Comparative evaluations show that the proposed framework achieves better overall performance than the existing denoising algorithms. Its advantage is most evident when the recordings are disturbed by severe baseline drift and complex non-stationary noise, in which case the TCDOA-optimized VMD provides effective signal-noise separation and the BiLSTM network retains the key diagnostic features. The improvement becomes less obvious when the input signal is already clean. One limitation is the relatively small sample size, which restricts the statistical generalization of the current findings. Another limitation is that, under extremely heavy noise, the network might potentially smooth out very weak features such as low-amplitude P-waves, which warrants further quantitative investigation.

The clinical reference is a clinician-selected pseudo ground truth, and this limits what the reported metrics can establish. The reference is a different window of the same recording and still contains residual noise; R-peak alignment removes only the bulk temporal offset, leaving residual misalignment and beat-to-beat variability; and it was chosen by

two clinicians without a formal inter-observer agreement analysis. The reported SNR, CosSim and RMSE should therefore be read as a relative ranking under a common reference rather than as absolute signal fidelity; an absolute reference would require simultaneous ECG, a physical phantom, or a multi-centre cohort.

Given its fundamentally modular architecture, the proposed framework demonstrates potential for future extension to other physiological signals or multimodal inputs. Furthermore, the high-fidelity signals recovered by the method establish a reliable foundation for downstream clinical tasks. Future work will build upon this denoising framework to construct precise 3D cardiac magnetic field maps and train automated CAD diagnostic models on a larger and more diverse clinical cohort. We will also continue to explore broader applications in the joint analysis of complex physiological signals.

Author Contributions: Conceptualization, K.Z. and J.D.; methodology, K.Z.; software, K.Z.; validation, K.Z. and B.Z.; investigation, J.W.; resources, K.Z., J.W. and B.Z.; writing—original draft, K.Z.; writing—review and editing, K.Z. and J.D.; visualization, J.W.; supervision, J.W., J.D. and B.Z.; project administration, J.D. and B.Z.; funding acquisition, J.D. and B.Z. All authors have read and agreed to the published version of the manuscript.

Funding: This research was funded by the National Natural Science Foundation of China, grant numbers 52175555 and 62501539.

Institutional Review Board Statement: This study was conducted in accordance with the ethical principles of the Declaration of Helsinki and was approved by the Medical Ethics Committee of Suzhou Dushu Lake Hospital (Approval No. 210048) on 2 August 2021.

Informed Consent Statement: The requirement for individual informed consent was waived by the Medical Ethics Committee of Suzhou Dushu Lake Hospital owing to the retrospective design of the study and the anonymized nature of the data. All data were anonymized and contained no personally identifiable information. The individual shown in Figure 1 is a junior colleague, and verbal informed consent for publication of the photograph was obtained.

Data Availability Statement: The data presented in this study are available on request from the corresponding author due to privacy and ethical restrictions.

Acknowledgments: During the preparation of this work, the authors used DeepSeek (version V3; accessed September 2026) to assist with reproducibility auditing and language editing. The authors independently reviewed and verified the source code, experimental outputs, statistical analyses, figures, and final text and take full responsibility for the content of this publication.

Conflicts of Interest: The authors declare no conflicts of interest.

Abbreviations

The following abbreviations are used in this manuscript:

MCG	Magnetocardiography
ECG	Electrocardiography
CAD	Coronary Artery Disease
VMD	Variational Mode Decomposition
EMD	Empirical Mode Decomposition
IMFs	Intrinsic Mode Functions
LSTM	Long Short-Term Memory
BiLSTM	Bidirectional Long Short-Term Memory
DOA	Dream Optimization Algorithm
TCDOA	Tent Chaotic Dream Optimization Algorithm
ADMM	Alternating Direction Method of Multipliers
SNR_{imp}	Signal-to-Noise Ratio improvement

CosSim	Cosine Similarity
RMSE	Root Mean Square Error
MSE	Mean Squared Error
BW	Baseline Wander
PLI	Power Line Interference
FIR	Finite Impulse Response
RPSEMD Soft	Regenerative Phase Shifted Empirical Mode Decomposition with Soft Thresholding
RPSEMD Hard	Regenerative Phase Shifted Empirical Mode Decomposition with Hard Thresholding
SGMD WT	Symplectic Geometry Mode Decomposition combined with Wavelet Thresholding
DRSN	Deep Residual Shrinkage Network

References

1. Wadhera, R.K.; Dhruva, S.S.; Bikdeli, B.; Bonaca, M.P.; Kittleson, M.M.; Ko, D.T.; Lu, Y.; Pagidipati, N.J.; Sawano, M.; Spatz, E.S.; et al. Cardio vascular statistics in the United States. JACC Stats. *J. Am. Coll. Cardiol.* **2026**, *87*, 1094–1134. https://doi.org/10.1016/j.jacc.2025.12.027.
2. Chong, B.; Jayabaskaran, J.; Jauhari, S.M.; Chia, J.; Le Roux, C.W.; Mehta, A.; Dimitriadis, G.K.; Chen, Y.; Toh, S.A.; Manla, Y.; et al. The Global Syndemic of Modifiable Cardiovascular Risk Factors Projected From 2025 to 2050. *J. Am. Coll. Cardiol.* **2025**, *86*, 165–177. https://doi.org/10.1016/j.jacc.2025.04.061.
3. Li, J.; Shen, Y.; Shen, C.; Ning, X.; Xiang, M. Advances of magnetocardiography in application of adult and fetal cardiac diseases. *Front. Cardiovasc. Med.* **2025**, *12*, 1522467. https://doi.org/10.3389/fcvm.2025.1522467.
4. Fenici, R.; Picerni, M.; Fenici, P.; Brisinda, D. Progress in Clinical Magnetocardiography: The Contactless Breakthrough for Noninvasive Clinical Detection of Cardiac Ischemia Now Needs Worldwide Standardization**.** *Sensors* **2026**, *26*, 1369. https://doi.org/10.3390/s26041369.
5. Lee, Y.H.; Kwon, H.; Kim, J.M.; Yu, K.K. The latest trend in magnetocardiogram measurement system technology. *Prog. Supercond. Cryog.* **2020**, *22*, 1–5. https://doi.org/10.9714/PSAC.2020.22.4.001.
6. Wacker-Gussmann, A.; Tardelli, G.; Cuneo, B.F.; Strasburger, J.F.; Wakai, R.T. Fetal Conduction Disease and Arrhythmia in Ebstein's Anomaly and Tricuspid Valve Dysplasia Assessed by Fetal Magnetocardiography. *J. Am. Heart Assoc. Cardiovasc. Cerebrovasc. Dis.* **2025**, *14*, e043614. https://doi.org/10.1161/JAHA.125.043614.
7. Tolstrup, K.; Akhtari, M.; Brisinda, D.; Meloni, A.M.; Siegel, R.J.; Fenici, R. Accurate diagnosis of ischemic heart disease without exposure to radiation using non-stress unshielded magnetocardiography. *Am. Heart J. Plus Cardiol. Res. Pract.* **2025**, *49*, 100483. https://doi.org/10.1016/j.ahjo.2024.100483.
8. Bao, B.; Hua, Y.; Wang, R.; Li, D. Quantum-Based Magnetic Field Sensors for Biosensing. *Adv. Quantum Technol.* **2023**, *6*, 2200146. https://doi.org/10.1002/qute.202200146.
9. Zhang, M.; Wang, Y.; Li, P.; Zhang, Y.; Xiang, M. Performance Evaluation of Magnetocardiography Sensor Arrays via Cramér–Rao Bound for Cardiac Source Localization. *IEEE Trans. Instrum. Meas.* **2025**, *74*, 1–10, 4016310. https://doi.org/10.1109/TIM.2025.3604125.
10. Van Veen, B.; Stenroos, M.; Wakai, R.T. Greedy Optimization of Sensor Array Geometry for Magnetocardiographic Source Localization. *IEEE Trans. Biomed. Eng.* **2025**, *72*, 1848–1857. https://doi.org/10.1109/TBME.2024.3524374.
11. Jia, Y.; Pei, H.; Liang, J.; Zhou, Y.; Yang, Y.; Cui, Y.; Xiang, M. Preprocessing and Denoising Techniques for Electrocardiography and Magnetocardiography: A Review. *Bioengineering* **2024**, *11*, 1109. https://doi.org/10.3390/bioengineering11111109.
12. Xing, Z.; Li, H.; Dou, H.; Zheng, Z.; Dai, J.; Wang, C.; Cui, J.; Zhang, X.; Jiang, T. Multi-Level Gated U-Net for Denoising TMR Sensor-Based MCG Signals. In *Proceedings of Medical Image Computing and Computer Assisted Intervention—MICCAI 2025, Dajeon, Republic of Korea, Part III*; Springer Nature: Cham, Switzerland, 2026; pp. 428–437.
13. Midani, W.; Ltif, H.; Ayed, M.B. A Comprehensive Review of Noise Removal Techniques in ECG Signal Processing. *Procedia Comput. Sci.* **2025**, *270*, 4134–4143. https://doi.org/10.1016/j.procs.2025.09.538.
14. Xing, B.; Feng, X.; Zhang, B. Research on Denoising Methods for Magnetocardiography Signals in a Non-Magnetic Shielding Environment. *Sensors* **2025**, *25*, 6096. https://doi.org/10.3390/s25196096.
15. Alves, B.; Simicic, D.; Mosso, J.; Lê, T.P.; Briand, G.; Bogner, W.; Lanz, B.; Strasser, B.; Klauser, A.; Cudalbu, C. Noise-reduction techniques for 1H-FID-MRSI at 14.1 T: Monte Carlo validation and in vivo application. *NMR Biomed.* **2024**, *37*, e5211. https://doi.org/10.1002/nbm.5211.

16. Surya, D.U.; Pramono, S.H.; Mudjirahardjo, P.; Muslim, P.A. Balancing Noise Reduction and Signal Preservation in EEG Signal for Mental Stress Detection Through Comparative Analysis of Filtering Techniques. In *Proceedings of the 2024 Beyond Technology Summit on Informatics International Conference (BTS-I2C), Jember, East Java, Indonesia*; IEEE: New York, NY, USA, 2024; pp. 41–46. https://doi.org/10.1109/BTS-I2C63534.2024.10942088.
17. Ádám, N.; Val'ko, D.; Balogh, Z.; Madoš, B.; Hurtuk, J. Comparative evaluation of filtration techniques for ECG signal denoising with emphasis on stationary wavelet transform. *Sci. Rep.* **2025**, *15*, 42514. https://doi.org/10.1038/s41598-025-26476-1.
18. Fatimah, B.; Singhal, A.; Singh, P. ECG arrhythmia detection in an inter-patient setting using Fourier decomposition and machine learning. *Med. Eng. Phys.* **2024**, *124*, 104102. https://doi.org/10.1016/j.medengphy.2024.104102.
19. Liang, S.; Qi, J.; He, J.; Jia, Y.; Wang, A.; Zhao, T.; Wei, C.; Jiao, H.; Feng, L.; Cheng, H. A Novel Adaptive Independent Component Analysis Method for Multi-Channel Optically Pumped Magnetometers' Magnetocardiography Signals. *Biosensors* **2025**, *15*, 243. https://doi.org/10.3390/bios15040243.
20. Zhang, J.; Song, X.; Jia, L.; Long, T.; Sun, H.; Zheng, C.; Chen, K.; Qi, S.; Zhou, B.; Liu, G. Three-dimensional visualization of MCG signals using CW_FastICA and transfer function mapping. *Measurement* **2026**, *273*, 121175. https://doi.org/10.1016/j.measurement.2026.121175.
21. Sayedelahl, M.A.; Farouk, R.M.; Adam, A.M. Enhancing biomedical signals through genetic algorithm optimized Exponentiated transmuted weibull denoising techniques. *Sci. Rep.* **2026**, *16*, 13409. https://doi.org/10.1038/s41598-026-46088-7.
22. Yang, S.; Wu, H.; Liao, X.; Lin, Y.; Chen, J. Empirical mode decomposition in clinical signal analysis: A systematic review. *Comp. Biol. Med.* **2025**, *194*, 110566. https://doi.org/10.1016/j.compbiomed.2025.110566.
23. Yu, H.; Baek, S.; Lee, J.; Sohn, I.; Hwang, B.; Park, C. Deep Neural Network-Based Empirical Mode Decomposition for Motor Imagery EEG Classification. *IEEE Trans. Neural Syst. Rehabil. Eng.* **2024**, *32*, 3647–3656. https://doi.org/10.1109/TNSRE.2024.3432102.
24. Pan, Z.; Xu, B.; Chen, W.; Fan, D.; Meng, X.; Peng, M.; Zhou, C. Improved Complete Ensemble Empirical Mode Decomposition with Adaptive Noise and Its Application in Noise Reduction for Fiber Optic Sensing. *J. Light. Technol.* **2025**, *43*, 2466–2474. https://doi.org/10.1109/JLT.2024.3489953.
25. Sun, M.; Wu, J.; Wang, Y.; Lu, Y.; Yu, F. DEP-CEEMDAN-MPE-INHT a time-frequency analysis method for noisy blasting seismic waves with adaptive noise suppression and endpoint processing. *Sci. Rep.* **2025**, *15*, 34934. https://doi.org/10.1038/s41598-025-18686-4.
26. Wang, M.; Xu, W.; Chen, S.-H.; Feng, J. On the end effect and end condition methods of empirical mode decomposition with cubic spline. *Commun. Nonlinear Sci. Numer. Simul.* **2026**, *153*, 109532. https://doi.org/10.1016/j.cnsns.2025.109532.
27. Dragomiretskiy, K.; Zosso, D. Variational mode decomposition. *IEEE Trans. Signal Process.* **2014**, *62*, 531–544. https://doi.org/10.1109/TSP.2013.2288675.
28. Yan, M.; Chen, L.; Hu, W.; Sun, Z.; Zhou, X. Secure and Intelligent Single-Channel Blind Source Separation via Adaptive Variational Mode Decomposition with Optimized Parameters. *Sensors* **2025**, *25*, 1369. https://doi.org/10.3390/s25041107.
29. Wang, D.; Tong, Y.; Yang, D.; Wang, P.; Lu, J. Optimized variational mode decomposition denoising method based on weighted mean of vectors algorithm. *Pet. Sci. Technol.* **2025**, *43*, 1–18. https://doi.org/10.1080/10916466.2024.2314182.
30. Zhou, Y.; Ma, Z.; Fu, L. A Review of Key Signal Processing Techniques for Structural Health Monitoring: Highlighting Non-Parametric Time-Frequency Analysis, Adaptive Decomposition, and Deconvolution. *Algorithms* **2025**, *18*, 318. https://doi.org/10.3390/a18060318.
31. Lian, S.; Li, Z. EEG motor imagery classification based on fusion of spatio-temporal attention and deep residual shrinkage temporal convolution. *Adv. Eng. Inform.* **2026**, *76*, 105050. https://doi.org/10.1016/j.aei.2026.105050.
32. Lin, J.; Zhang, J.; Cheng, J. Multi-Scale Residual Shrinkage Network with Adaptive Thresholding for Noise-Robust EEG Sleep Staging. *IEEE Access* **2026**, *14*, 85952–85972. https://doi.org/10.1109/ACCESS.2026.3700900.
33. Hu, L.; Cai, W.; Chen, Z.; Wang, M. A lightweight U-Net model for denoising and noise localization of ECG signals. *Biomed. Signal Process. Control* **2024**, *88*, 1746–8094. https://doi.org/10.1016/j.bspc.2023.105504.
34. Chorney, W.; Wang, H.; He, L.; Lee, S.; Fan, L. Convolutional block attention autoencoder for denoising electrocardiograms. *Biomed. Signal Process. Control* **2023**, *86*, 1746–8094. https://doi.org/10.1016/j.bspc.2023.105242.
35. Habutsu, T.; Nishio, Y.; Sasase, I.; Mori, S. A Secret Key Cryptosystem by Iterating a Chaotic Map. In *Advances in Cryptology—EUROCRYPT '91, Lecture Notes in Computer Science*; Springer: Berlin, Heidelberg, 1991; Volume 547, pp. 127–140. https://doi.org/10.1007/3-540-46416-6_11.

36. Lang, Y.; Gao, Y. Dream Optimization Algorithm (DOA): A novel metaheuristic optimization algorithm inspired by human dreams and its applications to real-world engineering problems. *Comput. Methods Appl. Mech. Eng.* **2025**, *436*, 117718. https://doi.org/10.1016/j.cma.2024.117718.
37. Hochreiter, S.; Schmidhuber, J. Long Short-Term Memory. *Neural Comput.* **1997**, *9*, 1735–1780. https://doi.org/10.1162/neco.1997.9.8.1735.
38. Schuster, M.; Paliwal, K.K. Bidirectional recurrent neural networks. *IEEE Trans. Signal Process.* **1997**, *45*, 2673–2681. https://doi.org/10.1109/78.650093.
39. Lee, D.; Shin, S.R.; Yeo, E.; Chung, W. Denoising sparker seismic data with Deep BiLSTM in fractional Fourier transform. *Comput. Geosci.* **2024**, *184*, 105519. https://doi.org/10.1016/j.cageo.2024.105519.
40. Jeong, S.; Chung, W.; Lee, D.; Park, J.; Bae, H. Effective noise suppression for Southern resident killer whale recordings using Transfer-Learned stacked BiLSTM. *Mar. Geophys. Res.* **2026**, *47*, 8. https://doi.org/10.1007/s11001-025-09605-3.
41. Md-Billal, H.; Syed Khairul, B.; Jesus, L.; Natasa, R.; Yeonsik, N.; Chon Ki, H. A Robust ECG Denoising Technique Using Variable Frequency Complex Demodulation. *Comput. Biol. Med.* **2020**, *126*, 104032. https://doi.org/10.1016/j.cmpb.2020.105856.
42. Tamaki, W.; Tsuda, E.; Hashimoto, S.; Toyomasa, T.; Fujieda, M. Magnetocardiographic recognition of abnormal depolarization and repolarization in patients with coronary artery lesions caused by Kawasaki disease. *Heart Vessel.* **2019**, *34*, 1571–1579. https://doi.org/10.1007/s00380-019-01383-4.
43. Podder, P.; Khan, T.Z.; Khan, M.H.; Rahman, M.M. Comparative performance analysis of Hamming, Hanning and Blackman window. *Int. J. Comput. Appl.* **2014**, *96*, 1–7. https://doi.org/10.5120/16891-6927.
44. Das, N.; Chakraborty, M. Performance analysis of FIR and IIR filters for ECG signal denoising based on SNR. In *Proceedings of the 2017 3rd IEEE International Conference on Research in Computational Intelligence and Communication Networks (ICRCICN*), *Kolkata, India*; IEEE: New York, NY, USA, 2017; pp. 90–97. https://doi.org/10.1109/ICRCICN.2017.8234487.
45. Wang, C.; Kemao, Q.; Da, F. Regenerated phase-shifted sinusoid-assisted empirical mode decomposition. *IEEE Signal Process. Lett.* **2016**, *23*, 556–560. https://doi.org/10.1109/LSP.2016.2537376.
46. Luan, J.; Chen, Y.; Zhang, H.; Xu, P.; Zou, L.; Wang, H. Research on vital sign detection methods based on improved regenerated phase-shifted sinusoid-assisted empirical mode decomposition. In *Proceedings of the Proc. SPIE 13653, Fifth International Conference on Digital Signal and Computer Communications (DSCC 2025), Changchun, China*; SPIE: Bellingham, WA,USA, 2025; p. 1365305. https://doi.org/10.1117/12.3071227.
47. Xing, T.; Ding, K.; Wang, X.; Wang, X.; Ni, K.; Zhou, Q. Hydrophone joint denoising based on the PSO-SGMD-WT method. *Measurement* **2025**, *255*, 117630. https://doi.org/10.1016/j.measurement.2025.117630.

Disclaimer/Publisher's Note: The statements, opinions and data contained in all publications are solely those of the individual author(s) and contributor(s) and not of MDPI and/or the editor(s). MDPI and/or the editor(s) disclaim responsibility for any injury to people or property resulting from any ideas, methods, instructions or products referred to in the content.